BNL-NUREG-26464



# INCEPTION AND DEVELOPMENT OF VOIDS IN FLASHING LIQUIDS*

by

Owen C. Jones, Jr.
Nuclear Safety Programs - Department of Nuclear Energy
Brookhaven National Laboratory, Upton, New York 11973

June 1979

ABSTRACT

This paper summarizes recent work aimed at correctly describing nonequilibrium vapor generation rates in flashing liquids in decompressing flows similar to those which might be encountered in a loss of coolant accident in a nuclear reactor. Analysis is reviewed which describes the flashing inception superheat in terms of the turbulence intensity for a given expansion rate and initial temperature, and interfacial area density and interfacial heat flux, and the volumetric vapor generation rates. Comparisons with existing data are included and further experiment being undertaken are described including typical recent results.

Manuscript Prepared for Presentation at the Joint
U.S. - Japan Information Exchange on Two-Phase Flow Dynamics
Osaka University, Osaka, Japan
August 1-3, 1979

*Work performed under the auspices of the U.S. Nuclear Regulatory Commission

# INCEPTION AND DEVELOPMENT OF VOIDS IN FLASHING LIQUIDS*

by

Owen C. Jones, Jr.
Nuclear Safety Programs - Department of Nuclear Energy
Brookhaven National Laboratory, Upton, New York 11973

June 1979

ABSTRACT

This paper summarizes recent work aimed at correctly describing nonequilibrium vapor generation rates in flashing liquids in decompressing flows similar to those which might be encountered in a loss of coolant accident in a nuclear reactor. Analysis is reviewed which describes the flashing inception superheat in terms of the turbulence intensity for a given expansion rate and initial temperature, and interfacial area density and interfacial heat flux, and the volumetric vapor generation rates. Comparisons with existing data are included and further experiment being undertaken are described including typical recent results.

Manuscript Prepared for Presentation at the Joint
U.S. - Japan Information Exchange on Two-Phase Flow Dynamics
Osaka University, Osaka, Japan
August 1-3, 1979



*Work performed under the auspices of the U.S. Nuclear Regulatory Commission

TABLE OF CONTENTS

## LIST OF FIGURES

LIST OF FIGURES (Continued)

LIST OF FIGURES (Continued)

## LIST OF TABLES

## NOMENCLATURE

### English

| | |
|---|---|
| $A_c$ | cross section area of pipe |
| $a$ | thermal diffusivity |
| $C_o$ | void distribution parameter |
| $C_T$ | parameter in Eq. (7) |
| $c$ | static quality |
| $c_p$ | specific heat at constant pressure |
| $d$ | diameter |
| $F_i$ | flashing index |
| $G$ | mass flux |
| $G_g$ | mass flow rate of vapor |
| $g$ | gravitational acceleration |
| $h$ | heat transfer coefficient (Eq. 6) or, enthalpy, (Eqs. 13 and 15) |
| $J$ | nucleation rate |
| $K_s$ | constant in Eq. (5) |
| $k$ | thermal conductivity |
| $L$ | latent heat |
| $m(z,\zeta)$ | mass of a vapor bubble at $z$ nucleated at $\zeta$ |
| $N$ | number density |
| $p$ | pressure |
| $q_i''$ | interfacial heat flux |
| $r$ | radius |
| $T$ | temperature |
| $t$ | time |
| $u$ | velocity |
| $u',v',w'$ | velocity fluctuation components |
| $U_o$ | Channel mass-averaged velocity |
| $V_{gj}$ | vapor drift velocity |
| $x$ | flowing quality |
| $z$ | spatial coordinate along pipe centerline in flow direction |

### Greek

| | |
|---|---|
| $\alpha$ | void fraction |
| $\beta$ | void fraction functional |
| $\Sigma'$ | rate of pressure decrease (expansion rate) |
| $\Gamma_v$ | volumetric rate of vapor mass generation |
| $\zeta$ | dummy variable of integration |
| $\xi_h$ | pipe perimeter |
| $\rho$ | mass density |
| $\sigma$ | surface tension |
| $\mu$ | viscosity |
| $\Delta$ | difference |

## Subscripts

| | |
|---|---|
| b | bubbles |
| d | droplets |
| f | saturated liquid phase |
| $F_i$ | flashing inception |
| $F_{io}$ | flashing inception under static conditions |
| g | saturated vapor phase |
| in | test section inlet |
| l | liquid |
| m | mixture |
| max | maximum |
| min | minimum |
| NVG | point of net vapor generation |
| o | initial point |
| rm | reduced minimum |
| s or sat | saturation |

## Superscripts

| | |
|---|---|
| * | dimensionless |
| ' | fluctuation |
| - | averaged |

## 1. INTRODUCTION

The transfer and conversion of energy utilizing fluid systems will continue to be emphasized during the next few decades at least, in spite of the progress currently being made in direct conversion technology. Because of the highly intensive transfer and conversion efficiency achieved through the utilization of latent heat interchange, multiphase flows will continue to play a central role in such systems. In many cases, nonequilibrium effects are important and must be considered.

The general way in which the problem on nonequilibrium phase change enters into questions of energy transfer is through the need to provide constitutive relations describing the actual rates of liquid-vapor mass exchange during non-ideal phase change processes. It is well known that, except in the most simplistic of cases, analysis of multiphase flow systems must begin with a minimum of four field equations, three each describing transfers of mass, momentum, and energy for the mixture, and one at least specifying conservation of mass for an individual phase, (or equivalent). The vapor continuity equation may be written as

$$\frac{\partial}{\partial t}\ (\alpha\rho_v) + \vec{\nabla} \cdot (\alpha\rho_u \vec{V}_v) = \Gamma_v \tag{1}$$

and depends heavily on the formulation utilized for the volumetric rate of vapor generation, $\Gamma_v$. Under conditions of thermodynamic equilibrium, $\Gamma_v$ is easily specified. However, under more complex situations such as during rapid flashing of superheated liquid into vapor due to decompression, the determination of the volumetric mass transfer rate, $\Gamma_v$, may be exceedingly difficult. It is the purpose of this paper to summarize the concerns regarding flashing flows and to present recent results applicable to these concerns.

## 2. ANALYSIS

Discounting the nucleation process itself as a mechanism for forming vapor, mass exchange between phases will occur at preexisting liquid-vapor interfaces. Examination of the microphenomena of the interfacial transfer yields an expression for the evaporative mass flux given by [1].

$$G_{lv} = \frac{\sum_{k=l,v} \vec{q}''_k \cdot \vec{n}_k + \sigma\nabla_s \cdot U_s - \sum_{k=l,v} (\bar{\bar{\tau}} \cdot \vec{n}_k) \cdot (\vec{U}_k - \vec{U}_s)}{\Delta i_{fg} + \frac{1}{2}\vec{U}_r \cdot \sum_{k=l,v} (\vec{U}_k - \vec{U}_s)} \tag{2}$$

For most practical engineering systems, only the first term in the denominator is important and relative kinetic exchange can be ignored. Also, net interfacial heat flux is generally predominant in relation to surface energy storage or dissipation. Thus, the evaporative mass flux is given solely in terms of the net interfacial heat flux as

$$G_{lv} = \frac{1}{\Delta i_{fg}} \sum_{k=l,v} \vec{q}''_k \cdot \vec{n}_k \cdot \qquad (3)$$

Application to an infintesimal volume along a streamtube yields a general expression for the vapor source term

$$\Gamma_v = \frac{1}{A_c \Delta i_{fg}} \int_{\xi_i} \sum_{k=l,v} \vec{q}''_k \cdot \vec{n}_k \frac{dA}{dz} \qquad (4)$$

Thus, it is readily seen that a mechanistic description for the volume vapor source requires description of both the net interfacial heat flux, $\vec{q}''_k \cdot \vec{n}_k$ and the interfacial area density, dA/dz. In addition, direct integration of equation (1) in the steady state case results in

$$x\rho_v v_v = \int_{\xi_o}^{\xi} \Gamma_v \, d\xi \qquad (5)$$

readily shows the importance of defining the point of net vaporization, $\xi_o$, in obtaining the correct description for the vapor mass flux. The same logic also applies to the transient situation.

It is well known for instance that the mass flow rates in critical flow conditions are highly dependent on the vapor content of the flow. Saha[2] has reviewed and evaluated critical flow research concluding that currently accepted equilibrium models underpredict critical flows for "short" pipes especially for subcooled or nearly saturated sources. While thermal nonequilibrium must be taken into account for "short" pipes, it is not clear how the combination of length and diameter enters the picture. Wu et al.[3] have shown that a model based on spherical bubble growth in fields of variable superheat adequately predicts the data of Reocreux[4] for void fractions less than 0.3. These predictions require accurate knowledge of both the voiding inception point and an initial nucleation density parameter. It is well known[5] that the initial degree of superheat markedly affects bubble growth in both constant and variable pressure fields. The degree of superheat has also been shown to play a strong role in void development in flashing critical flows[3]. Since the point at which flashing inception occurs directly affects the initial superheat, the flashing inception can also be expected to play a strong role in the critical mass flow rates under flashing conditions.

## Flashing Inception

Little work has been accomplished examining the point of flashing inception. Seynhaeve, Giot, and Fritte[6] ran experiments with inlet temperatures between 111° and 167°C and at mass fluxes between 10 and 20 $Mg/m^2$-s. They determined the superheat at flashing inception to behave inversely with mass flux. Although their data were quite scattered, the superheat apparently decreased to almost zero at the high mass fluxes, and even became negative

in a few cases. In their evaluation of Reocreux's 1.74 bar data, Wu et al[3] found similar results as shown in Figure 1. In this figure the superheat is expressed in terms of the overexpansion at the inception point denoted by $\Delta p_{fi}$. (Note that throughout this paper the terms overexpansion and superheat are used interchangeably and are, of course, coupled along the saturation line). Apparently no other experiment appears to have been here-to-fore undertaken allowing suitable definition for determination of flashing inception superheats.

The boiling inception and onset of net vapor generation in flowing liquids has been the subject of much scrutiny in the case of heating, having been the subject of such well known works as those of Hsu[7], and of Saha and Zuber[8], among others. Unfortunately, flashing inception does not appear to be characterized by models applicable to heated liquids where the superheat is generally confined to the wall layer in bulk subcooled liquids. Instead, bulk superheating occurs prior to flashing inception while the initial voiding still seems generally relegated to the wall layer.

In the case of static liquids undergoing rapid decompression, the situation appears quite similar. The work of Lienhard, Alamgir, and Trela[9] appears clearly applicable where the very early stages of blowdown were observed starting with pressures up to the 150 bar range and temperatures up to nearly 330°C. They found that the limit of overexpansion depends on the rate of decompression prior to nucleation up to a value of about 65% of the spinodal limit. This limit itself depends on the initial fluid temperature. They further suggest that various imperfections in cleaning and preparation of a given system as well as history of preparation may play a role. On the other hand the correspondence between their data and those of Edwards and O'Brien[10] makes this seem somewhat unlikely.

The data of Edwards and O'Brien[10] and of Lienhard, Alamgire, and Trela[8] occur with decompression rates of 0.05 - 1.5 Mbar/s while the data of Reocreux[4] and of Seynhaeve, Giot, and Fritte[6] decompress at rates three orders of magnitude slower. Decompression times in the static systems of References [9] and [10] data are generally less than a millisecond. Decompression times in the flowing systems of [4] and [6] range up to several tens or hundreds of milliseconds. The only other differences between the static and dynamic flashing systems seem to be those of fluid motion. Of the factors influenced by these motions, the turbulent pressure fluctuations appear to be those most likely to have an effect. Indeed, Chen[11] offered a similar suggestion to explain sodium boiling superheat behavior.

It thus seems that decompressive flashing inception might be characterized by at least three considerations: initial temperature; decompression rate; degree of liquid turbulence.

This section shall characterize using these ideas, flashing inception in flowing systems to the extent possible in view of the limited data available. Indeed, it will be shown that the inverse mass flux effects of both References [4] and [6] may be explained due to effects of turbulent fluctuations.

Conceptual Description. In view of the preceeding remarks, it appears that the condition of the fluid at the onset of flashing either static or flowing, might be characterized in terms of the turbulent pressure fluctuations. In the static systems of References [9] and [10], it is not likely that turbulence had time to develop.

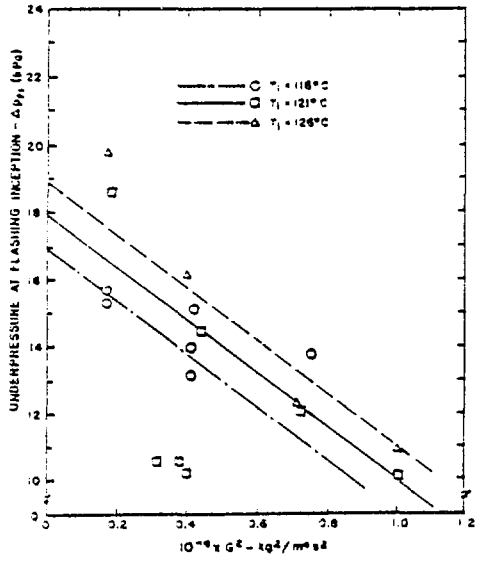


Figure 1. Observed mass flux effect on overexpansion (underpressure) at flashing inception for the data of Reocreux[3]. (BNL Neg. No. 3-237-79)

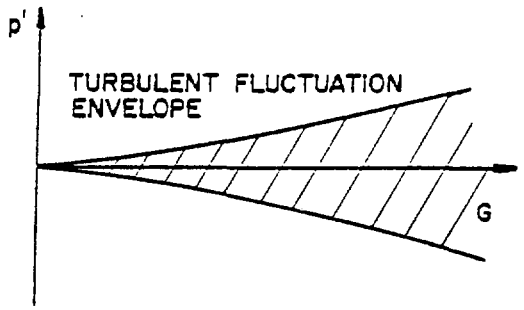


Figure 2. Sketch of pressure fluctuation envelope with varying mass flux. (BNL Neg. No. 3-239-79)

In the flowing systems of References [4] and [6], fully developed turbulence was most certainly present at the high Reynolds numbers encountered (order of $10^5$). The following hypotheses thus seem reasonable:

1. static flashing overexpansion is a function only of initial temperature and expansion rate, and represents the true inception potential, (Lienhard's hypothesis[8]);

2. dynamic flashing overexpansion at inception is subject to the additive effects of turbulence giving an apparent alteration in the inception potential.

It is suggested that the overexpansion at flashing inception may be expressed as

$$\Delta p_{Fi} = f\left[\Delta p_{Fio}(T_i, \dot{T}), p'\right] \tag{6}$$

where $\Delta p_{Fio}(T_i, \dot{T})$ is the overexpansion under zero flow conditions as dependent on initial temperature, $T_i$, and expansion rate, and $\dot{T}$, and $p'$ is the pressure fluctuation. Note that $T_i$ may be replaced with the spinodal limit $T_m$ after Lienhard et al[9] without loss of generality.

To see how the pressure fluctuations might enter into the picture, the fluctuation envelope may be envisioned as sketched in Figure 2 depending on the mass flux. As the flux increases, so does the turbulence intensity. According to the hypotheses, the bottom of the envelope would represent the true minimum

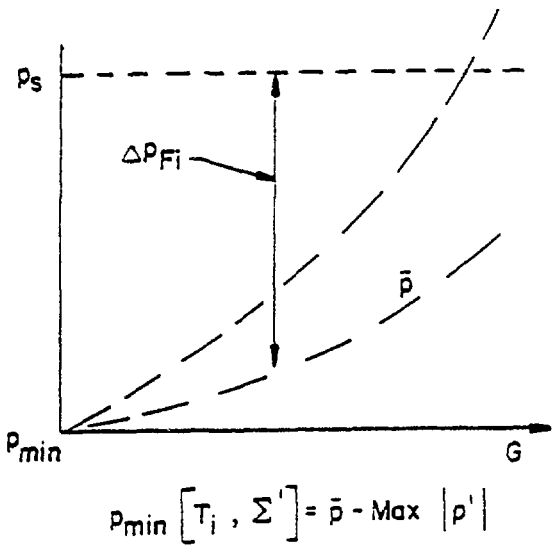


Figure 3. Qualitative effects of pressure fluctuations on observed overexpansion at flashing inception. (BNL Neg. No. 3-239-79)

pressure at any mass flux. If this minimum pressure is taken as identical to the static value at inception represented by hypothesis (1), then the average pressure at the inception point would have to increase with increasing mass flux as shown in Figure 3. Since the overexpansion at inception is the difference between the saturation pressure and the observed average pressure, this value, $\Delta p_{Fi}$, is seen to decrease in accordance with observation. If we define the apparent overexpansion at flashing inception as

$$\Delta p_{Fi} \equiv p_s - \bar{p}_{Fi} \tag{7}$$

and the true value is taken to be identical with the static value as

$$\Delta p_{Fio} \equiv p_s - p_{min} \tag{8}$$

then the relationship between the two, in view of Figures 2 and 3 is simply

$$\Delta p_{Fi} = \Delta p_{Fio} - \text{Max}\ |p'| \tag{9}$$

Note that the importance of turbulent pressure fluctuations in cavitation has been previously recognized by Daily and Johnson [12]. They, in fact, point out that the effects of dissolved gas or pre-existing gas nuclei will be to reduce the cavitation or flashing inception superheat.

Kinetic Description. The maximum in the pressure fluctuation envelope is assumed to coincide with the maximum kinetic fluctuations so that

$$\text{Max } |p'| = \frac{1}{2} \rho_\ell \left(u'^2_{max} + v'^2_{max} + w'^2_{max}\right) \tag{10}$$

The nucleation density monotonically increases with increasing superheat while the probability density of the kinetic energy fluctuations first increases then decreases. The product of nucleation density and superheat probability density is expected to yield a maximum with increasing superheat. This maximum would probably represent the inception point and is expected to fall within the 99% probability band. If the maximum fluctuation in each velocity component is thus assumed to be represented by the three sigma value, (three standard deviations), then

$$\text{Max } |p'| = \frac{1}{2} \rho_\ell \left(3\sqrt{\overline{u'^2}}\right)^2 + \left(3\sqrt{\overline{v'^2}}\right)^2 + \left(3\sqrt{\overline{w'^2}}\right)^2 \tag{11}$$

so that, for the case of isotropic turbulence (9) becomes

$$\Delta p^*_{Fi} \equiv \frac{p_{Fi}}{p_{Fio}} = 1 - 27 \left(\frac{\overline{u'^2}}{U_o^2}\right) \frac{G^2}{2\rho_\ell \Delta p_{Fio}} \tag{12}$$

It is thus seen that the apparent superheat at flashing inception in flowing systems may be expected to scale with the reduced limit of superheat, the expansion rate, the flashing index (reciprocal of the cavitation index), and the Reynolds number through the turbulent fluctuation intensity. Thus,

$$\Delta p_{Fi} = f(\Delta T_{rm}, \Sigma'^*, Re, F_i) \tag{13}$$

where

$\Delta T_{rm}$ = difference between the nucleation temperature and the saturation temperature at the same pressure, reduced to the critical temperature,

$\Sigma^*$ = dimensionless expansion rate (decompression rate)

$R_e$ = Reynolds number given by $R_e = U_o d\rho_\ell/\mu$

$F_i$ = flashing index given by $F_i = 1/2\rho_\ell U_o^2/\Delta p_{Fio}$.

There does not seem to be a readily apparent reference to nondimensionalize the expansion rate.

## Net Interfacial Heat Flux and Area Density

A reformulation of (4) taking into account a population of bubbles (the low void condition) having been nucleated at different points along a stream tube yields

$$\Gamma_v(z) = \frac{\pi}{A_c \Delta i_{fg}} \int_{z_o}^{z} q''(z,z')\delta(z,z') \frac{dN}{dz} dz' \tag{14}$$

The nucleation site density, dN/dz, results in bubbles in $dV = A_c dz$ having different Lagrangian histories, resulting in different interfacial heat fluxes and bubble sizes. Jones and Zuber[13] developed expressions for heat flux and size of bubbles growing in variable pressure fields yielding

$$q_i'' = \frac{k_\ell F_o}{\sqrt{\pi a_\ell t}} + \frac{k_\ell}{\sqrt{\pi a_\ell}} \int_o^t \frac{f'(\eta)}{\sqrt{t-\eta}} d\eta \tag{15}$$

and

$$\frac{\delta}{2} \equiv R(t) = \left(\frac{\rho_{v0}}{\rho_v}\right)^{2/3} \left\{ R_0 + \cdots \right. \tag{16}$$

$$\cdots + \frac{K_s k_l \Delta T_s}{\rho_{v0} \Delta i_{fg} \sqrt{\pi \alpha_l}} \left[ 2\sqrt{t} + \frac{2}{3}\left(\frac{\Delta i_{fg}}{R T_0} - 1\right) \int_0^T \left(\frac{T_0}{T} - 1\right) \eta^{-1/2} d\eta \right]$$

$$\cdots + \frac{K_s k_l}{\rho_{v0} \Delta i_{fg} \sqrt{\pi \alpha_l}} \left[ \int_0^t \int_0^\eta \frac{F'(\xi)}{(\eta - \xi)^{1/2}} d\xi d\eta + \cdots \right.$$

$$\left. \left. \cdots + \frac{2}{3}\left(\frac{\Delta i_{fg}}{R T_0} - 1\right) \int_0^t \left(\frac{T_0}{T} - 1\right) \int_0^\eta \frac{F'(\xi)}{(\eta - \xi)^{1/2}} d\xi d\eta \right] \right\}$$

From a mechanistic viewpoint, reasonably accurate results were obtained in comparison with single bubble data and might even be obtained in the case of flashing if the population could be accurately identified. There is reason to expect that the latter could be accomplished due to the autocatalytic nature of decompressive bubble growth.[3,13] From a practical standpoint, the triple integration along bubble trajectories to obtain $\Gamma_v$ from (14)-(16) does not seem reasonable.

Since bubbles growing in a Lagrangian field having decompression occurring as $t^n$ will have bubble radius growth as $t^{n+1/2}$, the resulting void fraction growth from these bubbles will be as $t^{3(n+1/2)}$ a very strong function of time.[13] Thus, bubbles first nucleated in a decompressing population will strongly dominate the vapor source term. It seems reasonable, then, to initially treat the nucleation rate as a delta function leading, therefore, to uniformly sized, identical history bubbles at a given cross section. As a consequence, the bubble population density, interfacial area density, size and void fraction may all be related through

$$\frac{1}{A_c}\int_{\xi_1}\frac{dA}{dz} = \frac{6\alpha}{\delta} = \pi N_b \delta^2 \tag{17}$$

Similarly, since the bubbles are treated as identical in a given cross section, the net interfacial heat flux will also be identical at any location. For short decompression times especially appropos of critical flow situations, the heat flux is assumed to be described approximately through the well known expression

$$\sum_{k=1,v}\vec{q}''_k\cdot\vec{n}_\kappa \sim K_s\frac{k_\ell}{\sqrt{\pi a_\ell t}}(T_\ell - T_s) \quad \text{as } t\to 0 \tag{18}$$

where $K_s$ is the sphericity correction factor of $\sqrt{3}$, (Plesset and Zwick[15]), or $\pi/2$, (Forster and Zuber[16]). As seen in Figures 4a, (Data of Niino[17]), and 4b, (Data of Hewitt and Parker[18]), the approximation (in terms of the effective heat transfer for coefficient) is reasonable for short times.

Vapor Source Term

By combining equations (4), (17), and (18), one obtains

$$\Gamma_v(z) = K_s\left[36\pi N_b\right]^{1/3}\alpha^{2/3}\frac{k_\ell(T_\ell - T_s)}{\Delta i_{fg}\sqrt{\pi a_\ell t}} \tag{19}$$

where obviously t is the Lagrangian lifetime of the bubbles at z. In obtaining this expression, Saha[14] and Wu et al.,[3] recognizing that the population density could not be specified a priori, simply utilized a correlation coefficient to be determined from experiment so as to begin to identify trends. The expression thus used was

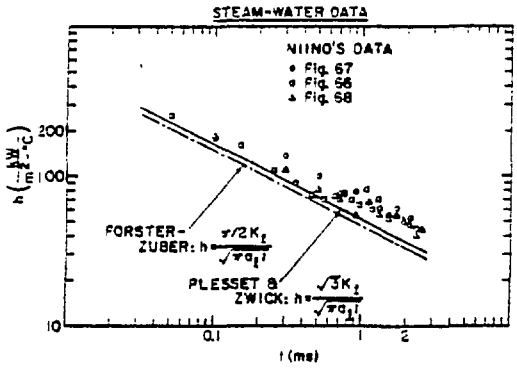


Figure 4a. Comparison of Plesset and Zwick (1954) and Forster and Zuber (1954, 1955) Heat Transfer Coefficient With Measured Instantaneous Heat Transfer Coefficient of Steam-Water During Variable Liquid Superheating.
(BNL Neg. No. 10-1596-78)

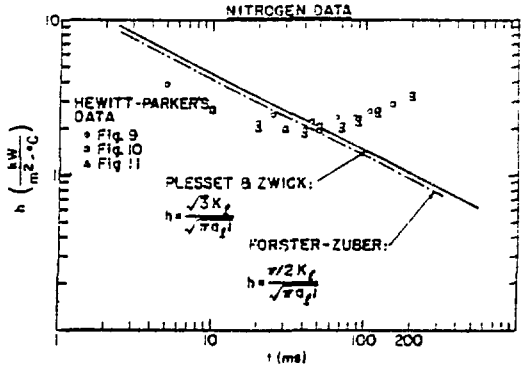


Figure 4b. Comparison of Plesset and Zwick (1954) and Forster and Zuber (1954, 1955) Heat Transfer Coefficient With Measured Instantaneous Heat Transfer Coefficient of Nitrogen During Variable Liquid Superheating.
(BNL Neg. No. 10-1596-78)

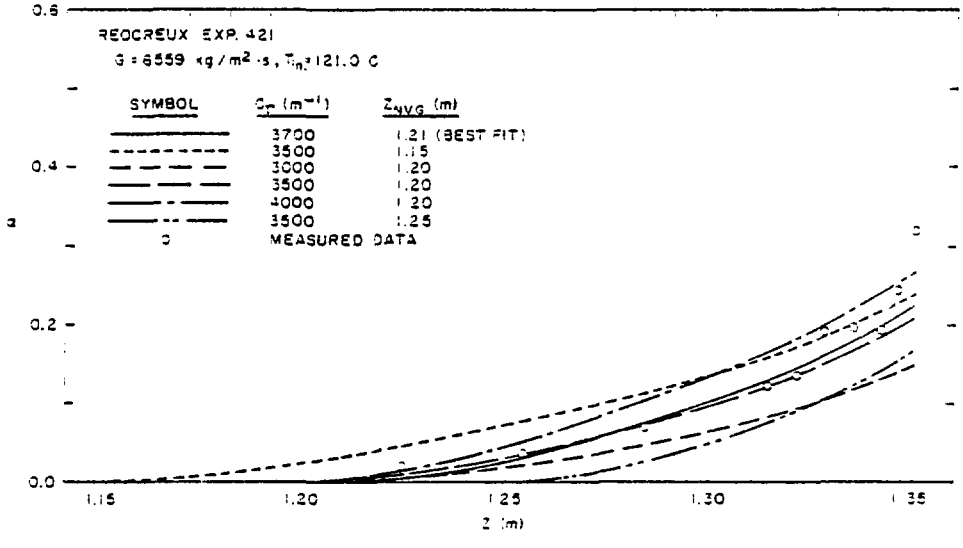


Figure 5. Variation of a $C_p$ with $C_p$ and $Z_{NVG}$ in Present Model and Comparison to Experimental Data of Reocreux. (BNL Neg. No. 10-1335-78)

$$\Gamma_v = C_\Gamma \frac{k_\ell}{\sqrt{a_\ell t}} \frac{(T_\ell - T_s)}{\Delta i_{fg}} \alpha^{2/3} \tag{20}$$

Note that while $C_\Gamma$ is dimensional having units of inverse length, its use at this juncture is intended simply as a guide to physical behavior and not for final correlation purposes.

Void and Quality Development

In steady homogeneous flow, the relation between the transport time and the coordinate along the centerline of the pipe in the flow direction is given by

$$dt = \frac{\rho_m}{G} dz \tag{21}$$

In order to integrate Eq. (20), the origin of the t-scale here is fixed at the point of net vapor generation, $z_{NVG}$, which may be specified as an input condition for each calculation. Along a streamline, Eq. (1) in steady state requires that

$$\frac{dx}{dt} = \frac{dx}{dZ} \frac{dZ}{dt} = \left(\frac{\Gamma_v}{G}\right)\left(\frac{G}{\rho_m}\right) = \frac{\Gamma_v}{\rho_m} \tag{22}$$

where $\rho_m$ is the local density of the two-phase mixture. Inserting Eq. (20) in Eq. (22), we have

$$x_2 - x_1 = \int_{t_1}^{t_2} \left[\frac{C_\Gamma k_\ell (T_\ell - T_s)\alpha^{2/3}}{\rho_m \sqrt{a_\ell}\, \Delta i_{fg}}\right] \frac{dt}{\sqrt{t}} , \tag{23}$$

where $x_1 = x(t_1)$ and $x_2 = x(t_2)$.

Given a value for the area-averaged actual vapor quality x and pressure, one can write the following expression for the area averaged void fraction $\alpha$:

$$\alpha = \frac{x}{C_o\, x + (1 - x)\frac{\rho_g}{\rho_\ell} + \frac{\rho_g V_{gj}}{G}} \tag{24}$$

where $\rho_g$ and $\rho_\ell$ are the vapor and liquid phase densities, and G is the mass-flux, $C_o$ is the void distribution parameter taken to be unity at this time, $V_{gj}$ is the vapor drift velocity, which is assumed to be given by the expression for bubbly churn-turbulent upflow (Kroeger and Zuber[20],

$$V_{gj} = 1.41\left[\frac{\sigma g(\rho_f - \rho_g)}{\rho_f^2}\right]^{1/4} \tag{25}$$

To calculate the locate liquid superheat, the assumption of adiabatic flow is made. In addition, since for the low pressure data currently available we are mainly interested in flows with low x values, ($x \lesssim 10^{-3}$), the contribution to energy balance from kinetic energy change may be ignored for flows in a constant area duct. Hence, the specific enthalpy of the flow may be assumed to remain unchanged. Thus,

$$h_m = ch_g + (1 - c)h_\ell = \text{const}, \tag{26}$$

where c, the static quality of the mixture, is given by

$$c = \frac{\alpha\rho_g}{(1 - \alpha)\rho_f + \alpha\rho_g} \tag{27}$$

and $h_m$, $h_\ell$ and $h_g$ are the enthalpies of the mixture, the liquid phase and the vapor phase respectively. Consistent with the assumption that the vapor is at the local saturation temperature, the vapor enthalpy is taken to be the saturation value corresponding to the local pressure. With $h_\ell$ from Eq. (13), the liquid superheat may be computed from

$$\Delta T \equiv T_\ell - T_s = \frac{h_\ell - h_f}{c_{p\ell}} \tag{28}$$

In the above, $h_f = h_f(p)$ is the saturated liquid enthalpy and $C_{p\ell}$ is the liquid specific heat.

Method of Integration

The quantity in the brackets in Eq. (23) is not expected to vary drastically within small step sizes ($t_2 - t_1$). Thus, a first order integration formula may be used, yielding

$$x_2 - x_1 = 2 < \left[\frac{C_1 k_\ell (T_\ell - T_s)\alpha^{2/3}}{c_m \Delta i_{fg} \sqrt{a_\ell}}\right] (\sqrt{t_2} - \sqrt{t_1}), \tag{29}$$

where < > signifies the mean value.

Now all the terms except $C_\Gamma$ in Eq. (20) are expressed as functions of the local pressure p. Therefore, if p(t) is known from experiments, $C_\Gamma$ may in principle be solved. In practice, however, an iterative procedure is adopted.

To perform the calculations, initial conditions, in particular $z_{NVG}$, and the void fraction $\alpha_o$ at this location must be known. We note that if the vapor nucleation rate could be calculated, both the location of the point of net vapor generation in the pipe and its void fraction could be determined by integrating the nucleation rate. In the absence of an applicable nucleation equation, values of $\alpha_o$ and $z_{NVG}$ must be assumed.

To determine the value of $C_\Gamma$ from experimental data, the following procedure may be used:

(i) Determine the point where the measured static pressure $p = p_{sat}(T_{in})$ where $T_{in}$ is the temperature at the test section inlet.

(ii) Set the constant in Eq. (26) to $h_{in}$, the enthalpy at the inlet, which is equal to the enthalpy corresponding to the saturated liquid at the pressure determined in (i).

(iii) Assume $\alpha_o$, $z_{NVG}$, and $C_\Gamma$ values.

(iv) Starting at $z = z_{NVG}$ and $\alpha = \alpha_o$, calculate the local pressure by interpolating the measured pressure distribution and calculate the local liquid superheat $\Delta T$, etc., from Eqs. (26)-(28).

(v) Increase z by step size $\Delta z$, and estimate $\Delta T$, etc. Take average.

(vi) Calculate new x from Eq. (29), and $\alpha$ from Eq. (24).

(vii) Evalute new superheat, etc., and compare with estimates in (v). Improve until convergence is reached.

(viii) Repeat (v)-(vii) until end of straight test section ($z = 1.351$ m) is reached.

(ix) Compare $\alpha(z)$ calculated with $\alpha(z)$ measured, change $\alpha_o$, $z_{NVG}$, and $C_\Gamma$ values and repeat (iii) to (ix) until agreement is reached.

## 3. RESULTS AND DISCUSSION

### Void Development

The point of flashing inception and net vapor generation are taken to be identical so that $z_{NVG}$ coincides roughly with the end of the nucleation zone, where a bubble population of $N_b$, with a certain average bubble size $\delta$, is generated. Since $C_\Gamma$ depends on $N_b$, and $\alpha_o$ is simply $(N_b \cdot \pi \delta^3/6)$, it is clear that $\alpha_o$, $z_{NVG}$, and $C_\Gamma$ are related and their values cannot be assigned independently of one another. Fortunately, it was found that the calculated void fraction distribution $\alpha(z)$ is not sensitive with respect to

changes in the values of $\alpha_o$ assumed in this model, and all calculations described herein were made with $\alpha_o = 0.00002$ regardless of the $C_\Gamma$ value. A step size of $\Delta z = 0.5$ mm was chosen after having passed the usual convergence test of the program.

Figure 5 shows results of a series of calculations performed on Exp. 421 reported by Reocreux[4]. We note that the curves of $\alpha(z)$ become steeper as $C_\Gamma$ is increased while $z_{NVG}$ is fixed, whereas they are translated downstream and steepen slightly as $z_{NVG}$ is increased for a constant $C_\Gamma$. These effects are to be expected physically since the vapor generation rate depends directly on $C_\Gamma$, whereas an increase in $z_{NVG}$ delays the flashing point, causing the ensuing bubble growth to occur under higher superheat conditions, resulting in a higher $\Gamma_v$. Assisted with these observations, one may then make judicious choices of $C_\Gamma$ and $z_{NVG}$ in order to achieve the best fit to the experimental data. For this experiment, the combination $C_\Gamma = 3700$ m$^{-1}$ and $z_{NVG} = 1.21$ m seems to yield the best agreement with the measurements.

The results of calculations which give the "best fit" to all experiments evaluated are summarized in Figs. 6, 7, and 8. It is seen that in general, the model works well for about $\alpha < 0.3$, but, at higher void fractions, it seems to under-predict the vapor generation rate. Maximizing the interfacial area density for a given $N_b$ did not lead to a sufficient increase in $\alpha$ to reconcile the difference shown in these figures. The interfacial area density was maintained constant for void fractions of 0.3 and larger in these calculations to account for possible transition to slug (churn turbulent) flow although if let to increase, only a slightly higher $\alpha$ value than those presented here are obtained. However, such an assumption on flow regimes is unrealistic (Dukler and Taitel[21]), and it only serves as an upper bound for estimating possible errors in $\Gamma_v$ due to errors in the $A_s$ assumptions. The discrepancy between the measured and calculated $\alpha$ may be attributed to the inadequacy of the conductive heat transfer model which is assumed to control the bubble growth rate, and in turn, the vapor generation rate. In the transition regime to bubbly-slug flow, relative motion of the phases may significantly improve the heat transfer rate raising the bubble growth rate over that predicted by the conduction-limited rate. Moreover, the $\alpha$-distribution measured by Reocreux represents diametrically averaged values of $\alpha$, not the cross-section averaged values calculated from the present model. For certain radial void distribution profiles, the diametrical average may be higher than the cross-sectional average void fraction.

Figure 9, (same data as in Fig. 1), exhibits the relationship of the quantity $(p_{sat} - p_{NVG})$ and the mass flux G. Since the liquid superheat at the point of net vapor generation is directly related to the pressure difference $(p_{sat} - p_{NVG})$, the latter may be taken as a measure of the maximum superheat sustained by the liquid before flashing occurs. On the other hand, variation of a liquid pressure with distance in the flow direction in a straight pipe scales as $(1/2)\rho u^2$, the time rate of pressure drop is then proportional to $(1/2)\rho u^3$, or, to $G^3$. Hence, Fig. 9 may be interpreted as displaying the effect of expansion rate on the limit of superheat determined from Reocreux's experiments. It is interesting to note that higher superheat (or $p_{sat} - p_{NVG}$) was reached for low expansion rates and lower superheat for higher expansion rates. This trend, which has also been observed by Seynhaeve, et al.,[6], is exactly opposite to that found in supersonic flows with vapor condensation where the critical supersaturation [the counterpart of $(p_{sat} - p_{NVG})$ here] attained is inversely related to the vapor cooling rate (counterpart of expansion rate here).

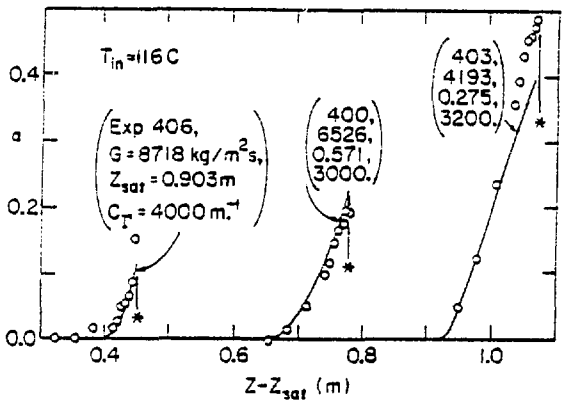


Figure 6. Void Fraction Distribution in a Constant Area Channel as a Function of Mass Flux G. $T_{in} \approx 116$ C. o, Measurements by Reocreux (1974); ____, Calculations Based on the $C_\Gamma$ Values Shown. (BNL Neg. No. 10-501-78)

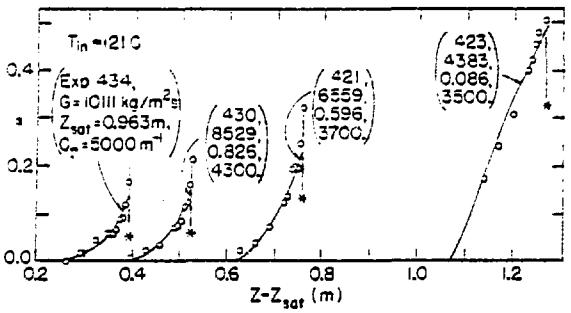


Figure 7. Void Fraction Distribution in a Constant Area Channel as a Function of Mass Flux G. $T_{in} \approx 121$ C. o, Measurements by Reocreux (1974); ___, Calculations Based on the $C_\Gamma$ Values Shown. (BNL Neg. No. 10-504-78)

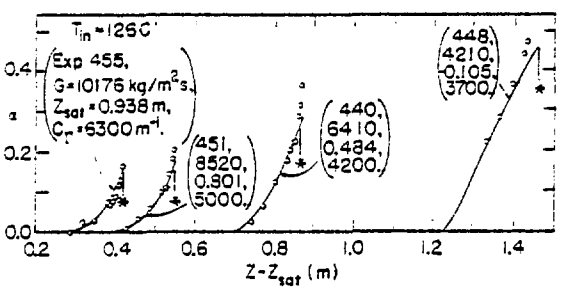


Figure 8. Void Fraction Distribution in a Constant Area Channel as a Function of Mass Flux G. $T_{in} \approx 126$ C. o, Measurements by Reocreux (1974); ___, Calculations Based on the $C_\Gamma$ Values Shown. (BNL Neg. No. 10-502-78)

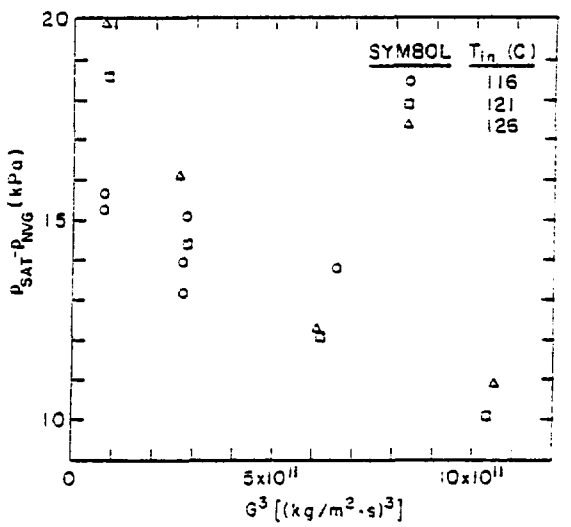


Figure 9. Effect of Expansion Rate on the Pressure at the Point of Net Vapor Generation. (BNL Neg. No. 10-1336-78)

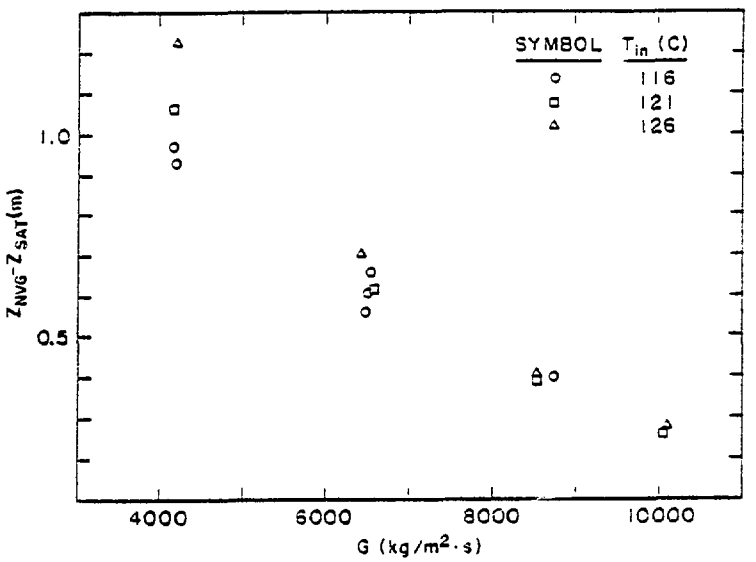


Figure 10. Variation of Point of Net Vaporation $z_{NVG}$ with Mass Flux G and Initial Temperature $T_{in}$ in Flashing Flow. Values of $z_{NVG}$ which give "best fit" to Reocreux's (1974) data. (BNL Neg. No. 10-1334-78)

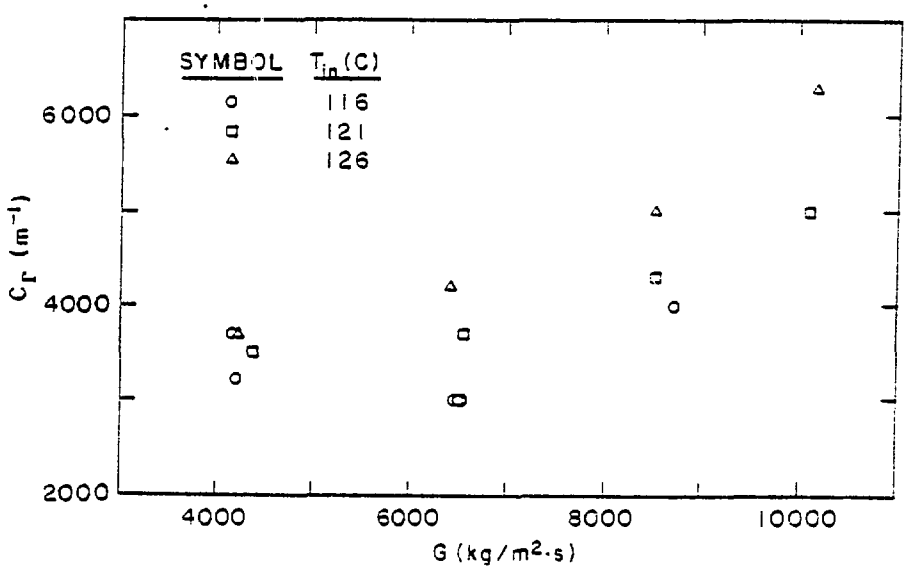


Figure 11. Variation of $C_r$ with Mass Flux G and Initial Temperature $T_{in}$ in Flashing Flow. Values of $C_r$ which give "best fit" to Reocreux's (1974) data. (BNL Neg. No. 10-1333-78)

Finally, the values of $z_{NVG}$ and $C_\Gamma$ determined from these experiments are presented as functions of the mass flux in Figs. 10 and 11. Again, a trend opposite to that found in condensing flows was found here in $z_{NVG} - z_{sat}$ curve. The trend of steadily increasing $C_\Gamma$ with G noted in Fig. 11 seems to be different from what one would expect based on the trend of $p_{sat} - p_{NVG}$ vs. G found in Fig. 9. A low value of $p_{sat} - p_{NVG}$, as found in the high G case, would give rise to a lower nucleation rate leading to a lower $C_\Gamma$, but a higher $C_\Gamma$ was found based on the current calculation method. The origin of this discrepancy is as yet not known.

We recall that the quantity $C_\Gamma$ incorporates the constant coefficients in Eqs. (17) and (18) in addition to $N_b^{1/3}$. Variations in $C_\Gamma$ may reflect the need to modify the conductive heat transfer coefficient adopted here. Contributions from convection, turbulent diffusion, etc., may significantly alter the heat transfer coefficient and $C_\Gamma$. These points are being investigated at present.

Eq. (12) shows that the apparent overexpansion at flashing inception should be linear in the square of the mass flux with an intercept of the static inception value, $\Delta p_{Fio}$. If the ideas previously expressed are at all valid, then using extrapolated values of $\Delta p_{Fio}$, turbulent fluctuation intensities obtained at known inception points should match those found, for instance by Laufer[19], of 0.07-0.08.

Figure 1 shows the data of Reocreux[4]. The straight lines in the figure represent an attempt to correlate the three sets of data in a consistant fashion and in a way that allows extrapolation to zero mass flux. The values of $\Delta p_{Fio}$ thus obtained were 17, 18, and 19 kPa, representative of actual superheats of approximately 3.5°C. Note that 1.0 kPa represents about 0.18°C at the conditions tested.

Using the values of $\Delta p_{Fio}$ obtained from Figure 1, the mean fluctuation intensities may be computed from the data. These are shown in Figure 12 (solid symbols). Also shown in this figure are the kinetic energy fluctuation intensities scaled appropriately for convenience of plotting, (open symbols). The average of the velocity fluctuation intensities obtained is 0.072 in good agreement with the measurements of Daily and Johnson[12] based on their measurements of bubble motion and also of Laufer[19]. No observable trend with mass flux is noticed. Also, there is surprisingly little scatter in the results so obtained.

Reocreux's data is replotted in Figure 13 on dimensionless coordinates suggested by Equation (12). Since the fluctuation effects are subtractive, Equation (12) suggests the possibility of negative superheats. This is shown by the x-intercept at a flashing index, $F_i$, of 7.2. While there is nothing actually prohibiting the turbulent pressure fluctuations from exceeding the values required to overcome the zero-flow incipient superheat, bubbles thus generated would probably collapse almost immediately in the bulk subcooled liquid unless carried to lower pressure regions before this could happen. An envelope of $\Delta p_{Fi}^*$ is thus suggested as

$$\Delta p_{Fi}^* = \text{Max} \begin{cases} 0 \\ 1-27\left(\dfrac{\overline{u'^2}}{U^2}\right) F_i \end{cases} \qquad (30)$$

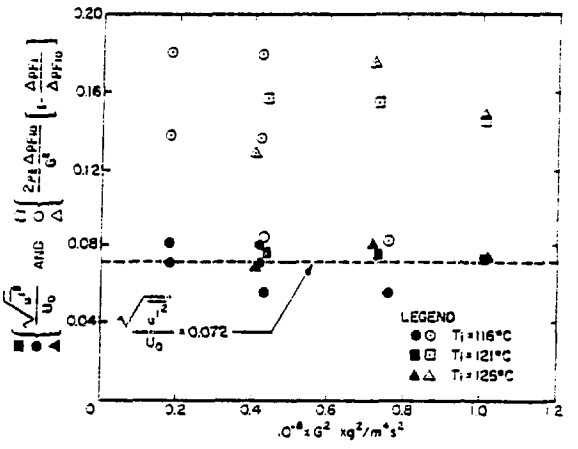


Figure 12 - Velocity and scaled kinetic energy fluctuation intensities calculated from the overexpansion data of Reocreux[4] at flashing inception.
(BNL Neg. No. 3-235-79)

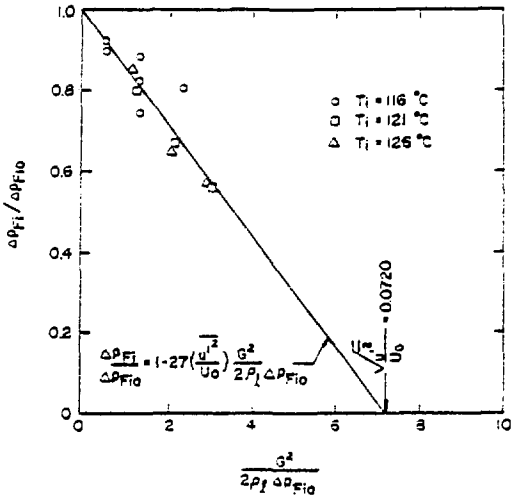


Figure 13- Dimensionless correlation of Reocreux's[4] overexpansion data at flashing inception.
(BNL Neg. No. 3-240-79)

Finally, extrapolative determination of $\Delta p_{Fi_0}$ for the data of Seynhaeve, Giot, and Fritte[6] would negate the validity of any other comparison. Thus, it is not possible to obtain a meaningful comparison of the majority of these data with the results of Equation (30). However, if there is any validity in the preceeding concepts, it might be expected that the Reference[6] data in the same temperature range as the Reocreux[4] data may exhibit the same behavior. Both sets of data are plotted in Figure 14. Also shown in this figure is the prediction based on a static inception underpressure of 18kPa. The trends observed appear to support the conclusions previously stated. Note that the lower limit of zero superheat also appears reasonable and tentatively supported by the relatively meager amount of data available.

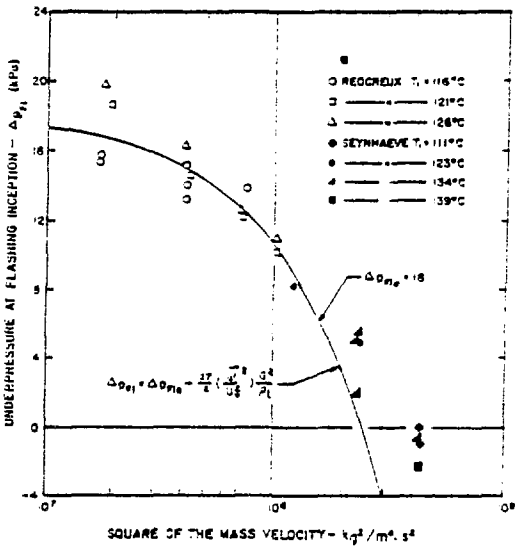


Figure 14 - Comparison of the flashing inception data of Reocreux[3] and of Seynhaeve, Giot, and Fritte[5] with the theory developed herein using the approximate static flashing overexpansion value of 18 kPa for the computation.
(BNL Neg. No. 3-238-79)

## 4. FURTHER EXPERIMENTS

To amplify and extend the existing data to higher pressures and to situations having higher steady state decompression rates than those of

Reocreux[4] and of Seynhaeve et al.,[6], experiments have been designed and are currently being undertaken as described below. Detailed information regarding these tests may be found in a recent report by Zimmer et al.[22].

## Test Facility

The main flow loop presented in Figure 15 is constructed from "three inch" nominal (7.6 cm) stainless steel pipe. High purity water is circulated through the loop using a centrifugal pump rated at 1500 ℓ/min at a head of 600 kPa. Continuous three mode feedback control of all facility parameters is utilized to achieve very stable, self regulated operation.

Starting from the pump, the fluid passes through a flow control and measurement station, (3 to 950 ℓ/min with an accuracy of 1/2 percent of reading), the heater system (≤ 520 kW with outlet temperature regulated to ± 0.3°C), and through the test section to a condensing tank where a cooling spray is utilized to condense the vapor and to fix the tank temperature.

After leaving the condensing tank, the fluid travels back to the pump, and, depending on conditions, cooling water from excess pump flow can be added to prevent cavitation in the pump.

A pressurizer may be used to fix the inlet pressure to the test section or, together with the condensing tank to also control the test section pressure drop. If isolated from the system, the condensing tank provides the major control for the loop pressure.

Purification of the test fluid is accomplished during initial filling of the test loop. The water is deoxidized, deionized and passed through 0.22 micron filters. In addition, about 40 ℓ/min of excess pump flow is passed through the purification station as a polishing procedure during flow loop operation to maintain neutral pH with resistivities up to 18 MΩ- cm.

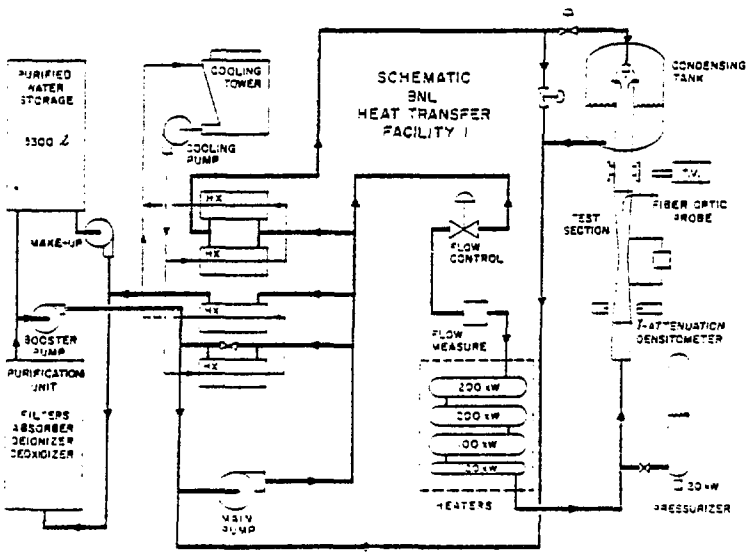


Figure 15 - Schematic of BNL Heat Transfer Facility (BNL Neg. No. 1-1246-79).

Operational ranges for the various loop parameters are shown in Table 1. Types of facility instrumentation and expected accuracies are identified in Table 2.

## Test Section

The test section shown in Figure 16 is made of stainless steel with a total length of 78.7 cm, including a symmetrical converging/diverging portion of 55.9 cm length and inside diameters of 5.1 cm at the ends and 2.5 cm at the throat. The wall thickness varies only from 0.57 mm to 0.60 mm over the entire tube length. Detailed mechanical inspection was used to determine that the mean deviation from design dimensions over the 66-cm shows that most of the measured dimensions deviate less than one-half a length centered at the throat was 0.21% with a standard deviation also of 0.21% and a maximum duration of 0.7% near the inlet. 49 wall pressure taps (0.4 mm in diameter) were installed in 1.27 cm centers along the length of the venturi, in addition to a set of observation windows located 30 cm downstream of the test section exit, which allowed photographic observations by flash photography. Taps 1-3 and 47-49 are in the constant area inlet and outlet sections respectively. An additional pressure tap, 50, located at 159 cm upstream of the test section inlet tap 1, is constantly monitored to provide absolute pressure at the test section inlet. Temperatures are monitored by means of two platinum resistance thermometers, one located near pressure Tap 50 for the flow inlet conditions and one at the condensing tank for the flow outlet conditions.

A single channel gamma densitometer which can be traversed virtually everywhere along the test section with an accuracy of $\pm$ 0.05 mm was added for axial and chordal measurements of void fraction.

## $\gamma$-Densitometer for Void Fraction Measurements

The single channel $\gamma$ densitometer schematic present in Figure 17 was used for the void fraction measurements. Thulium-170, obtained as 99.999 percent pure Thulium Oxide powder, sealed in an aluminum cylinder formed the basic material of the $\gamma$-source irradiated at the High Flux Beam Reactor at Brookhaven National Laboratory. Because of the need to keep the shielding weight on the traversing mechanism low, the source strength was kept at a few millicuries due to the presence of high energy-activity (1.12 MeV), which is due to trace amounts ( $\sim$70 ppm) of Scandium impurity. The beam was collimated to 2.5 mm diameter. The detector consisted of a Cadmium Telluride crystal (2.5 x 2.5 mm) mounted on a regular BNC connector, connected to "off-the-shelf" radiation electronic components (Tennelec), consisting of a preamplifier (TC 164), a high voltage power supply (TC 948) for the bias voltage (150 V), a linear amplifier (TC 203 BLR), a single channel analyzer (TC 440), a TC 541 Timer and a scaler (TC 540A). The single channel analyzer was used in the differential discriminator mode of operation and the energy window was set around 84 keV with a dispersion range of $\pm$ 10 keV. The TC 541 timer was altered by Tennelec to include time intervals as short as 0.1 msec and as long as 54 sec. Standard logarithmic calculational methods were used to determine void fractions from measurements made with reference to empty and full calibrations taking into account the normal half life decay of the source.

The calibration of the test section along the axis was performed with the test section empty and full of water at 20°C is compared with calculated values derived from the physical measurements of wall thickness and inside diameter along the nozzle in Figure 18. For these calculations, the attenuation coefficients for steel was taken as $\mu_{st}$ = 2.7 $cm^{-1}$ and for water

TABLE I

OPERATIONAL RANGE OF THE FACILITY

| | |
|---|---|
| Test Section Inlet Pressure | 100 - 1000 kPa |
| Test Section Inlet Temperature | 20-150°C |
| Mass Flux | 1.1 - 7.9 $Mg/m^2s$ |
| Reynolds Number Based on Inlet Conditions | $10^5$ -$10^6$ |

TABLE 2

TEST SECTION INSTRUMENTATION

| QUALITY MEASURED | TYPE OF SENSOR | RANGE | ACCURACY |
|---|---|---|---|
| Temperature | Resistance Temp. Detector (RTD) | -200 to 500°C | 1.2% @ 200°C |
| Differential Pressure | Strain Gage Δp Transducer | 4 to 500 kPa | 1% of Reading |
| Flow Rate | Turbine Meter | 3 to 950 ℓ/min | 0.5% reading |
| Void Fraction | Gamma Densitometer (Thulium/Cad-Telluride) | 0 to 1 | 5% Steady State (Future 5% per 1 ms, ~ 1% steady state) |

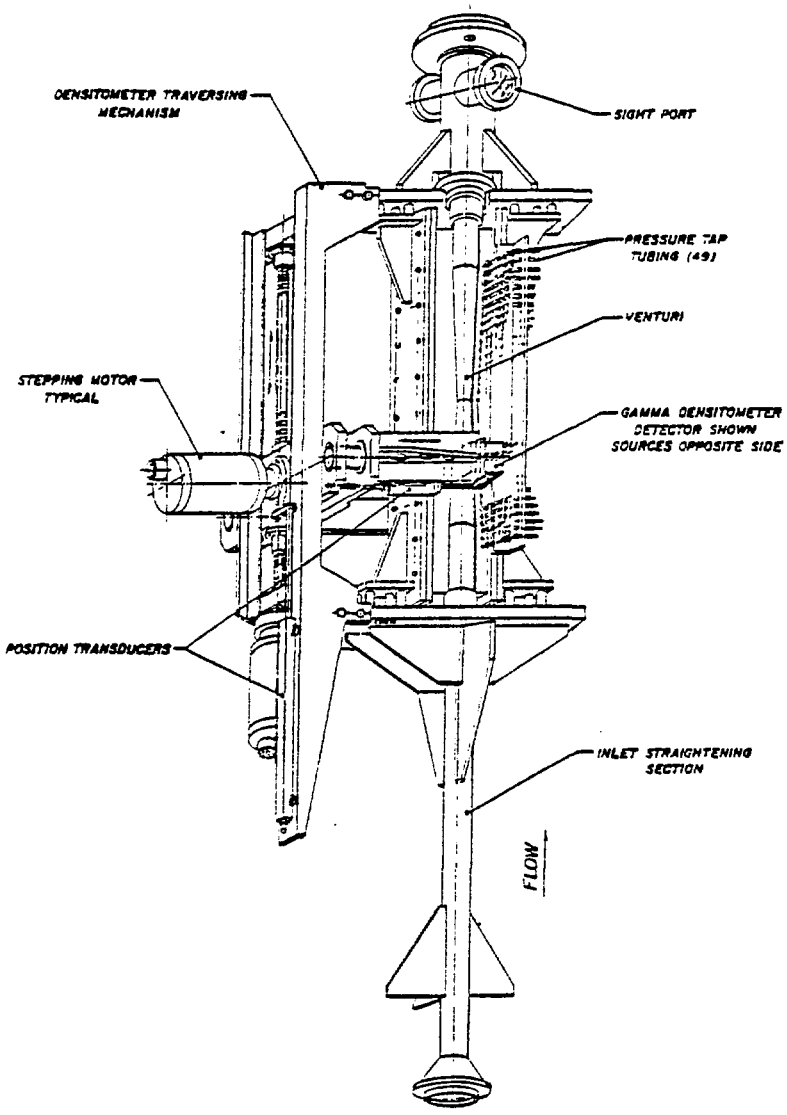


Figure 16 - Pictorial Drawing of TS-2 Test Section Used in BNL Flashing Experiments. (BNL Neg. No. 4-947-79)

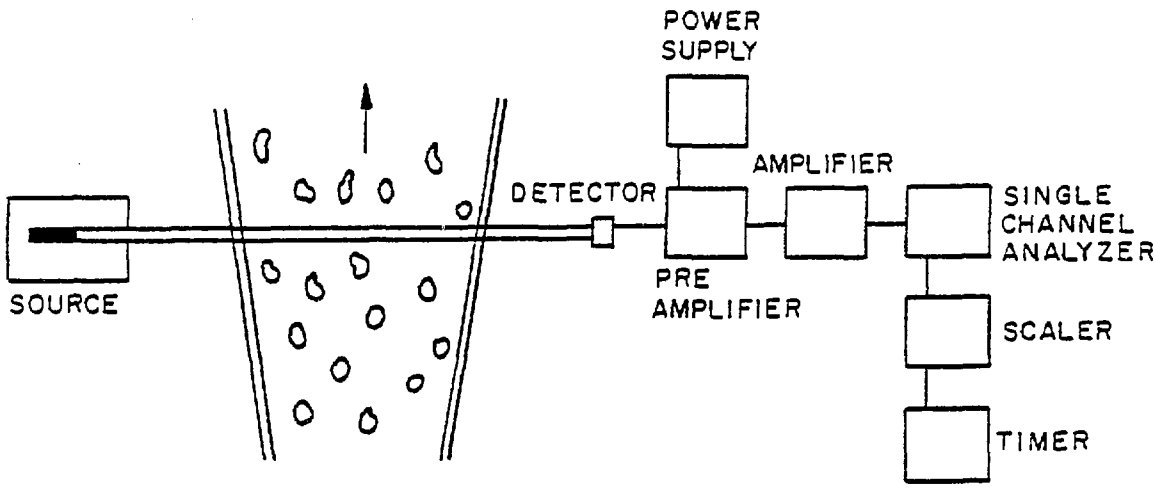


Figure 17 - Schematic Representation of γ-Densitometer (BNL Neg. No. 3-1016-79).

$\mu_w = 0.167\ cm^{-1}$, both values are listed for a 100 keV γ-energy level (Reactor Physics Constants, 1963). Repeatability of the results are within the expected standard duration as long as the source decay is taken into consideration. Radial calibration data were recorded at a single axial location (z = 183 mm) and are presented in Figure 19. The circles at R = 0, which is the axial Figure 18 location, corresponds to the calibration measurement reported in Figure 18 at z = 183 mm. The reproducibility of the results is very good. The standard deviations of ten consecutive measurements is shown as vertical bars in each figure and is within $1/\sqrt{I}$ yielding accuracy of the system ∿ 4 percent. Increasing the source strength in future tests to higher activity level should improve the statistical accuracy.

Data Acquisition

General Data Acquisition System. The centralized Data Acquisition and Data Analysis System (DADAS, Figure 20)) is used to obtain all data for these experiments including automatic positioning control and readout of nuclear data. This system was designed as a real time digital data system with multiterminal multiasking capability. The system was constructed around a Hewlett Packard 9640 system consisting of a 21MX minicomputer with 112 kilowords of central memory, 7.5 megaword cartridge discs, 9 track magnetic tape transport and paper tape I/O. Central control of the system is accomplished with a CRT terminal while the 3 satellite stations employ silent 700 terminals. Tabular and graphical presentation of data is achieved with a Varian electrostatic printer/plotter capable of listing 600 LPM and plotting 1.6 ips. Interface of the ADC systems is both direct, an interface per device, and via the universal interface bus, IEEE standard 488.

Three levels of ADC speed and resolution are incorporated within DADAS. The slow speed, high resolution system employs an integrating digital voltmeter with microvolt resolution and 300 channel guarded crossbar scanner. The through-put rate of this system is up to 18 measurements per second with high

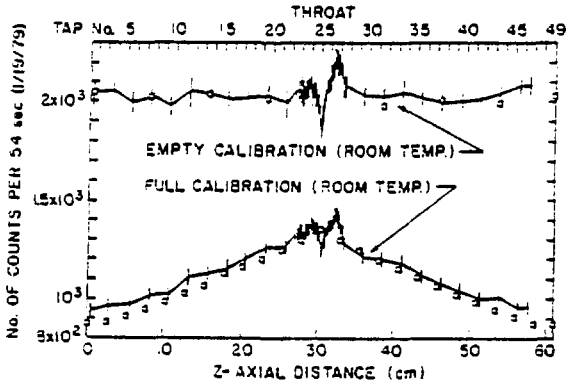


Figure 18. Calibration of the Test Section Both Empty (Air) and Full of Water as a Function of Axial Distance Compared with Calculated Valves. (BNL Neg. No. 3-1018-79)

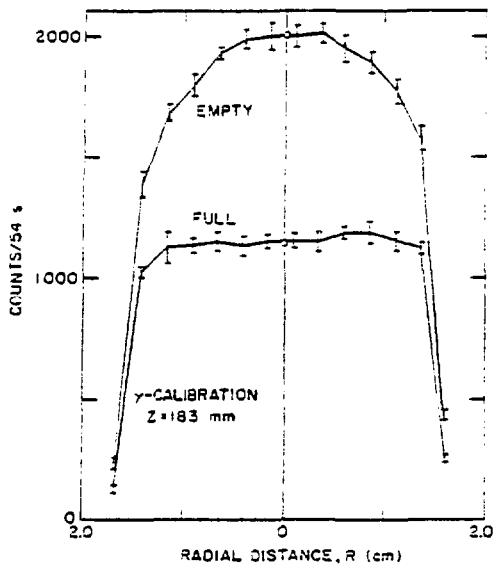


Figure 19. Calibration of the Test Section Both Empty (Air) and Full of Water as a Function of Radial Distance at a Fixed Axial Position (BNL Neg. No. 3-1020-79)

common mode voltage rejection capability. The intermediate speed system is a 15 bit (± 10.24 volts) multiplexed ADC with a 50 kHz through-put rate. The system employs a single programmable gain amplifier and a signal conditioning amplifier and filter per channel. The system has high common mode voltage rejection capability and can be connected directly to experiments. The high speed system is also a 15 bit (± 10.24 volt) multiplexed ADC with a 500 kHz through-put rate. The system has eight input channels with simultaneous sample and hold amplifiers. This system was designed specifically for digitizing analog tapes.

Static Pressure Measurement Set-Up. Each of the 49 pressure taps on the test section can be connected to either of two manifolds, one a common high side, the other a common low side, via two hand operated toggle valves to the low or high pressure sides of pressure transducer bank. The differential pressure between two locations along the test section can be measured by connecting the two taps to the low and high sides of the pressure transducer. Six Statham pressure transducers were used with the ranges of 17, 34, 69, 170, 340, and 690 kPa (2.5, 5, 10, 25, 50, 100 psi). These transducers are repetitively calibrated to a resolution of 1 part in 300,000 using a digital quartz manometer and bellows pressure source. They were connected in parallel to the two pressure measuring manifolds through two solenoid valves. A third solenoid valve in each transducer allows the shorting of the high and low pressure lines and thus provides means of measuring and monitoring the zero point stability of the transducer preceding every $\Delta p$ measurement. The solenoid valves are designed for a 200 psi differential pressure and were tested prior to installation. Once the two pressure taps were manually connected to the high and low pressure manifolds, the computer controlled procedure described below was initiated for the recording of the data.

FIGURE 20

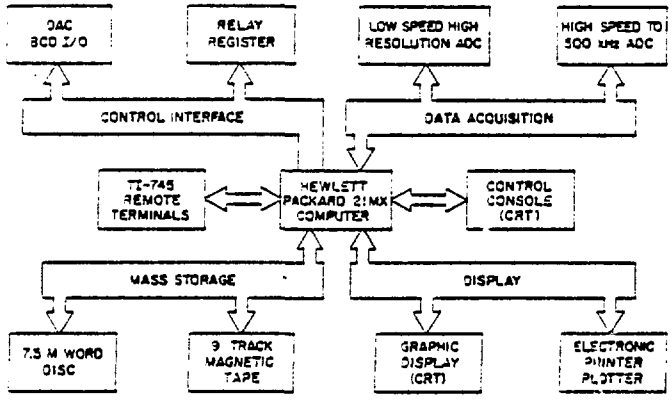


Figure 20. Block Diagram of Data Acquisition and Control System. (BNL Neg. No. 5-196-79)

Each measurement started with the pressure gauge shorted to record the zero Δp output. The pressure differential between the two taps was then measured across the 690 kPa (100 psi) range transducer. Once the pressure differential was calculated, the system automatically selected a pressure transducer such that the DP to be measured would fall between 25 and 75 percent of the full range of the particular transducer chosen. With the chosen transducer, the computer first measured the gauge's zero output when shorted, then took 20 consecutive DP readings, averaged them, and calculated their standard deviation. The same sequence was repeated once again and the new average of 20 new readings was compared to the last one calculated. If the two consecutive averages were within one percent of each other, the measurement was accepted and printed out as a data point. At the same time, the instantaneous flow rate and other flow variables of interest were also recorded. On the other hand, if the two consecutive averages did not satisfy the acceptance criterion, the computer repeated this procedure until the criterion was met or until 15 sets of 20 readings each were made and the last output was printed as the data point. This procedure permitted the measurement of static pressures with an accuracy of 1 percent of the reading as quoted in Table 2. It also allowed us to detect the presence of large pressure fluctuations at the onset of flashing or condensation. At other locations, such fluctuations were not observed and the readings converged smoothly.

## 5. TYPICAL EXPERIMENTAL RESULTS

### Pressure and Void Distributions

Pressure calibration for the venture is shown in Figure 21 representing 19 separate experiments covering the Reynolds number range of $\sim 10^5 - 10^6$. These data were used to obtain the effective area of the duct.

Typical results are shown in Figures 22-24. In Figure 22, data for flashing incepting just upstream of the throat are shown exhibiting a relatively constant pressure downstream of the throat indicating constant liquid velocity. The void fraction profile confirms this estimate increasing linearly due only to duct expansion filling with voids.

Figure 23, on the other hand, shows data with significant inlet voids and flashing with considerable overexpansion. Finally, in Figure 24, data are shown having delayed both expansion flashing followed by a partial pressure recovery indicating condensation confirmed by the void profiles. Much more severe condensation fronts have been observed as shown in Figure 25, all data obtained at $\sim 100°C$ but with mass fluxes between 1.81 and 6.01 $Mg/m^2s$.

### Determination of Vapor Source Terms

By utilizing the drift equations (24) and (25) and optimal spline fitting to the pressure and void data, the vapor generation rates may be obtained as shown in Figure 26. Note that there is little sensitivity to the drift velocity and distribution parameter at low void fractions, but at high void fractions, the discontinuity in equation (24) at $\alpha \sim 1/Co$ yields extreme sensitivites at high void fractions to choice of $C_o$. Note than values of $\Gamma_v$ obtained are quite similar to those obtained from Reocreux data[4].

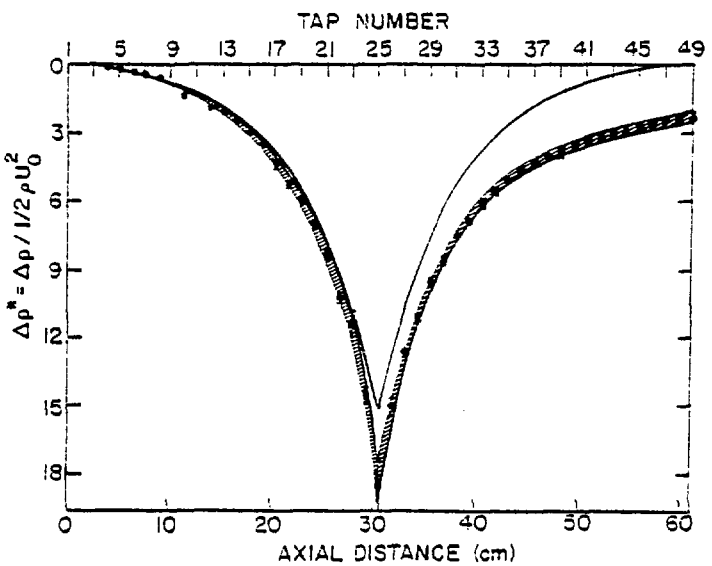


Figure 21. Dimensionless Pressure Distribution for TS-2. Data is averaged for all the Hydrodynamic Calibration Runs Performed.
(BNL Neg. No. 3-1022-79)

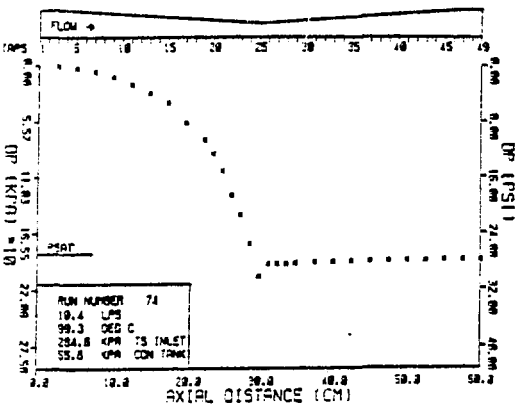


Figure 22a. Pressure and axial void fraction distributions in the test section. Plot of the difference between the dimensionelss measured pressure drop and the nondimensional pressure drop measured in the single phase calibration ($DDP = DP^*_m - DP^*_c$) as function of axial distance.
a) Pressure Profile
(BNL Neg. No. 3-1645-79).

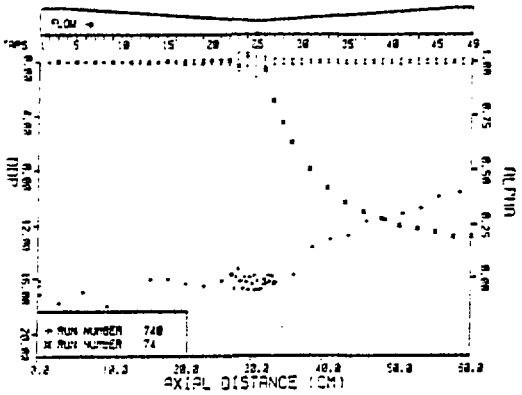


Figure 22b. b) Pressure Difference Profile and Axial Void Profile (centerline only) (BNL Neg. No. 3-1645-79)

## 6. CONCLUSIONS

a. Conduction-controlled vapor generation rates appear reasonable in modeling nonequilibrium flashing flows at low void fractions.

b. For void fractions lower than 0.3, the void development seems dependent only on voids formed at or upstream of the point of net vapor generation.

c. Flashing inception superheat has been found to vary inversely with mass flux and appears to be described by the effects of turbulent fluctuations, (Equation 21). This suggests that the flowing and static superheats at inception are identical once urbulent fluctuations are accounted for.

d. It is suggested that the limit of flashing inception with vanishing mass flux in flowing systems coincides with that value that would be obtained by static decompression at the same expansion rates.

e. The scaling parameters for flashing inception appear to be the reduced limit of superheat, $\Delta T_{rm}$, the Reynolds number, the flashing index (reciprocal of the cavitation number), and a dimensionless expansion rate. It is not clear, however, what reference quantities are reasonable to render the expansion rate dimensionless.

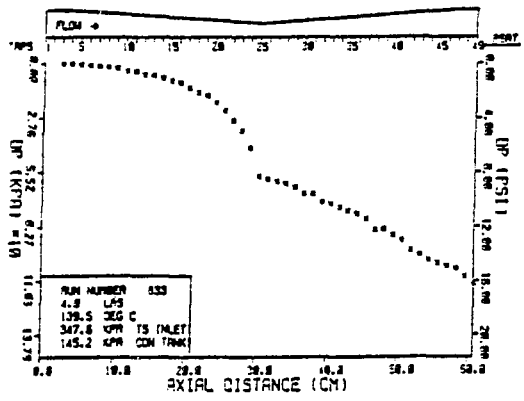


Figure 23a. Pressure and axial void fraction distributions in the test section with flashing occurring upstream of the nozzle throat. Plot of the difference between the dimensionless measured pressure drop and the nondimensional pressure drop measured in the single phase calibration, ($DPP = DP_m^* - DP_c^*$) as a function of axial distance.
a) Pressure Profile
(BNL Neg. No. 3-1109-79)

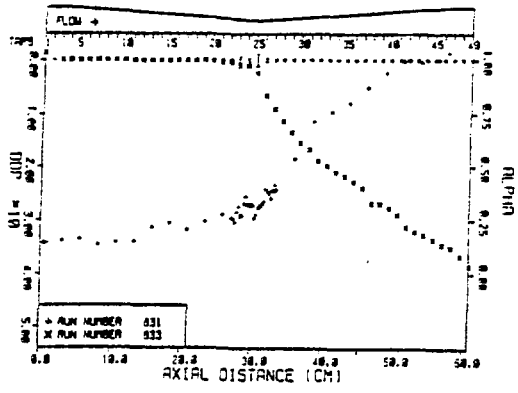


Figure 23b. b) Pressure Difference Profile and Axial Void Profile
(BNL Neg. No. 3-1109-79)

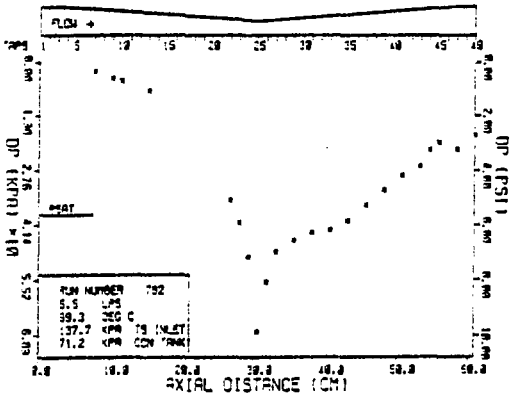


Figure 24a. Pressure and axial void fraction distributions in the test section. Plot of the difference between the dimensionless measured pressure drop and the nondimensionless pressure drop measured in the single phase calibration ($DDP = DP_m^* - DP_c^*$) as function of axial distance.
a) Pressure Profile
(BNL Neg. No. 3-1642-79)

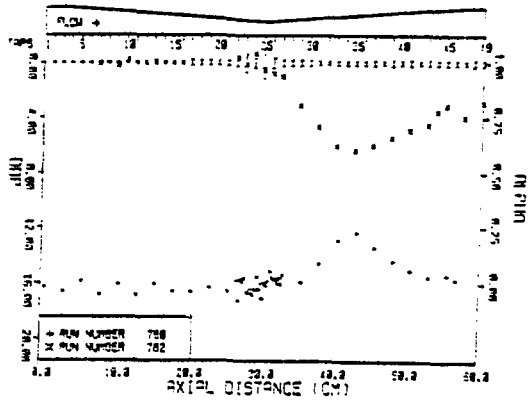


Figure 24b. b) Pressure Difference Profile and Axial Void Profile
(BNL Neg. No. 3-1642-79)

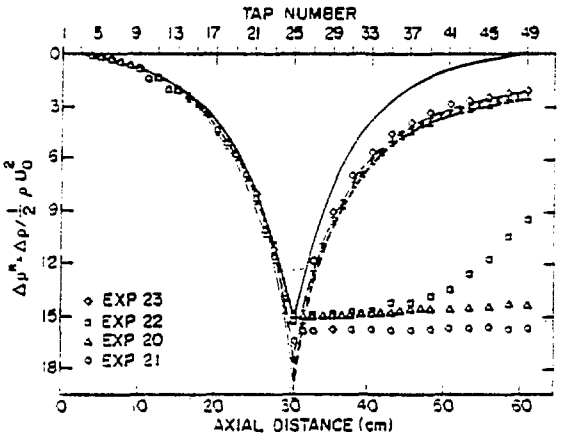


Figure 25. Dimensionless Pressure Distributions in TS-2 Under Flashing Conditions as Compared to Single-Phase Hydrodynamic Calibration Data (BNL Neg. No. 3-1021-79)

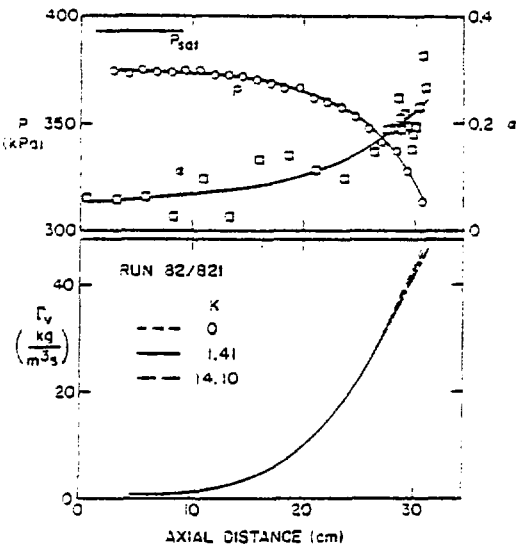


Figure 26. Determination of Non-equilibrium Flashing Vapor Generation Rates (BNL Neg. No. 3-1226-79)

f. Additional data are needed for flashing inception at higher pressures. Sufficient detail are required to accurately determine the inception point due to the sensitivity of void development to small changes in superheat at inception. Sufficient range in mass flux is required to allow extrapolative determination of the case of vanishing turbulence.

g. Analysis is needed to determine the behavior of the static flashing inception with expansion rate. The reasons for the observed behavior are not clear at this time.

h. A test facility has been constructed and experiments are being undertaken to further extend the data base for determination of the vapor source term. Quite accurate control and measurement of loop parameters is achievable, and measurements facilitated by automtic data acquisition methods.

i. A simple gamma densitometer has been developed and results shown for low activity sources. Higher activity sources have been activated and results are forthcoming.

## 7. ACKNOWLEDGEMENTS

This paper is a composite of work accomplished through the hard work and dedication of many people for whom the author is mainly a reporter. These people include N. Abuaf, G. A. zimmer, P. Saha, B.J.C. Wu, H. W. Kramer, W. J. Leonhardt, J. Klein, C. E. Schwarz, J. J. Barry, J. R. Klages, D. Becker, T. Feierabend, N. Schneider, and T. Rowland. In addition, the author is especially grateful for enlightening discussions with J. H. Lienhard of the University of Kentucky and Dr. R. Simoneau of NASA Lewis Research Center. This work was undertaken under the auspices of the U. S. Nuclear Regulatory Commission.

## 8. REFERENCES


[1] O. C. Jones, and P. Saha., "Non-Equilibrium Aspects of Water Reactor Safety," in Thermal Hydraulic Aspects of Nuclear Reactor Safety, O. C. Jones and S. G. Bankoff, ASME, New York, 1977.

[2] P. Saha, "A Review of Two-Phase Steam-Water Critical Flow Models with Emphasis on Thermal Nonequilibrium," BNL-NUREG-50907, September, 1978.

[3] B.J.C. Wu, P. Saha, N. Abuaf, and O. C. Jones, Jr., "A One Dimensional Model of Vapor Generation in Steady Flashing Flow," Interim Milestone Report, BNL-NUREG-25709, October, 1978.

[4] M. Reocreux, "Contribution a l'Etude des Debits Critiques en Ecoulement Diphasique Eau-Vapeur," PhD Thesis, Universite Scientifique et Medicale de Grenoble, France, 1974.

[5] O. C. Jones, Jr., and N. Zuber, "Bubble Growth in Variable Pressure Fields," Trans. ASME, J. Heat Trans., 100C, 453-459, 1978.

[6] J. M. Seynhaeve, M. M. Giot, and A. A. Fritte, "Nonequilibrium Effects on Critical Flow Rates at Low Qualities," Proc. of the CSNI Specialists Meeting on Transient Two-Phase Flow - Toronto, Canada, August 3-4, 1976.

[7] Y. Y. Hsu, "On the Size Range of Active Nucleation Cavities on a Heating Surface," Trans. ASME, J. Heat Trans., 84C, 207-216, 1962.

[8] P. Saha, and N. Zuber, "Point of Net Vapor Generation and Vapor Void Fraction in Subcooled Boiling," in Heat Transfer 1974, Proc 5th Int. Heat Trans. Conf., Vol IV, 175-179, 1974.

[9] J. H . Lienhard, Md. Alamgir, and M. Trela, "Early Response of Hot Water to Sudden Release from High Pressure," Trans. ASME, J. Heat Trans., 100C, 473-479, 1978.

[10] A. R. Edwards, and T. P. O'Brien, "Studies of Phenomena Connected with Depressurization of Water Reactors," J. Brit. Nucl. Ener. Soc., 9, 125-136, April, 1970.

[11] J. C. Chen, "Effect of Turbulent Flow on Incipient Boiling Superheat," Proc. 1st Mtg. of Technology Grp. on Liq. Metl. Thermal Sci., Brookhaven National Laboratory, May 1969.

[12] J. W. Daily, and V. E. Johnson, Jr., "Turbulence and Boundary Layer Effects on Cavitation Inception from Gas Nuclei, "Trans. ASME, 78 1695-1706, 1956.

[13] O. C. Jones and N. Zuber, "Bubble Growth in Variable Pressure Fields., Trans. ASME, J. Heat Trans., 100C, 453-459, (1978).

[14] P. Saha, "Reactor Safety Programs: Progress Report for the period April-June, 1977," BNL-NUREG-50683, p. 145, (1977).

[15] M. S. Plesset and S. A. Zwick, "The Growth of Vapor Bubbles in Superheated Liquids," J. Appl. Phys., 25, 493-500, (1954).

[16] H. K. Forster and N. Zuber, "Growth of a Vapor Bubble in a Superheated Liquid," J. Appl. Phys., 25, 474-478, (1954).

[17] M. Niino, "Study of Single Bubble Generation and Growth by Laser Beam," PhD Thesis, University of Tohoku, Japan, (1975).

[18] H. C. Hewitt and J. D. Parker, "Bubble Growth and Collapse in Liquid Nitrogen," Trans. ASME, J. Heat Trans., 90C, 22-26, (1968).

[19] J. Laufer, "Investigation of Turbulent Flow in a Two-Dimensional Channel," NALA-TN-2123, July, (1950).

[20] P. G. Kroeger and N. Zuber, "An Analysis of the Effects of Various Parameters on the Average Void Fractions in Subcooled Boiling," Int. J. Heat Mass Transfer, Vol. II, pp. 211-233 (1968).

[21] A. E. Dukler and Y. Taitel, "Flow Regime Transitions for Vertical Upward Gas-Liquid Flow: A Preliminary Approach Through Physical Modeling," NUREG-0162 (1977).

[22] G. A. Zimmer, B.J.C. Wu, W. J. Leonhardt, N. Abuaf and O. C. Jones, "Pressure and Void Distributions in a Converging-Diverging Nozzle with Nonequilibrium Water Vapor Generation," BNL-NUREG-26003, April, 1979.